Supplementary Information: Data Driven Analytics of Porous Battery Microstructures

Abhas Deva,[a] Vojtech Krs,[b] Lucas D. Robinson,[a] Carl S. Adorf,[c] Bedrich Benes,[b] Sharon C. Glotzer,[c] and R. Edwin García *[a]

[a]School of Materials Engineering, Purdue University, West Lafayette, Indiana 47907

[b]Department of Computer Graphics Technology and Department of Computer Science, Purdue University, West Lafayette, Indiana 47907

[c]Chemical Engineering, University of Michigan, Ann Arbor, MI 48109

*Contact author; phone:(765) 463-7801; email: redwing@purdue.edu

March 13, 2021

1 Material Parameters and Model Validation

Design adjustable and material parameters used in the electrochemical simulations are summarized in Table S1. Figure S1 compares the simulated voltage vs normalized capacity response for Li_xC_6 | LMO cell for spherical-shaped anode and cathode particles against the corresponding experimentally reported galvanostatic response by Doyle, Newman, and coworkers [1]. Calculations show an excellent agreement with the experimental voltage curves.

Table S1: Summary of parameters for dualfoil simulations. Parameter values are based on [1]

Parameter	Description	Anode	Cathode	Separator	Units
δ	Layer thickness	100	174	52	μm
ρ	Density of material	1.9	4.14	1.32	g/cm^3
ϵ_{liq}	Volume fraction of liquid phase	0.357	0.444	0.724	-
ϵ_{poly}	Volume fraction of polymer phase	0.146	0.186	0.276	-
ϵ_{fill}	Volume fraction of filler	0.026	0.076	-	-
c_s°	Initial lithium concentration	21.11	16.00	-	mol/dm^3
r_p	Effective particle radius	12.5	8.5	-	μm
D_s	Lithium diffusivity	3.9×10^{-10}	1.0×10^{-9}	4.0×10^{-6}	cm^2/s
$\sigma_\circ$	Electrical conductivity	1.0	0.038	a function, [2]	S/cm
$i_\circ$	Exchange current density	0.11	0.08	-	mA/cm^2
c_t	Lithium solubility	26.39	22.86	-	mol/dm^3
R_f	Film resistance	0.0	0.0	-	Ω/cm^2
Parameter	Description	Value			Units
α_{sep}	Bruggeman exponent of separator	3.3			-
c°	Initial salt concentration	2.0			mol/dm^3
T	Absolute Temperature	298.15			K
ρ_l	Density of liquid phase	1.324			g/cm^3
ρ_p	Density of polymer phase	1.780			g/cm^3
R_i	Additional residual resistance	97.345			Ω/cm^2

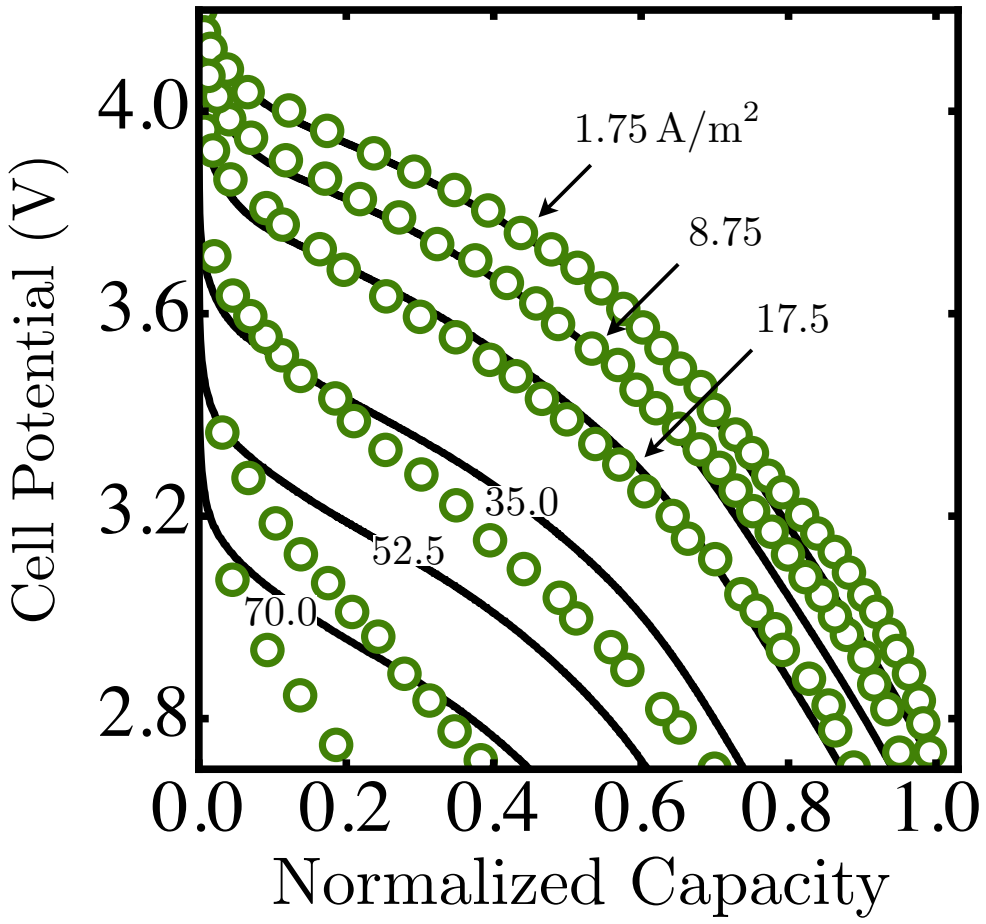

Figure S1: Calculated voltage vs normalized capacity response for Li_xC_6 | LMO cell for parameters as specified in Table S1 and selected current densities. Circles correspond to experiments by originally Doyle, Newman, and coworkers [1]. Solid lines correspond to the simulation results.

2 Effect of Texture

Microstructures approximated by morphologically anisotropic particles such as ellipsoids, show significant difference in the Bruggeman exponents in the through-thickness and in-plane directions [3]. Figure S2 shows five representative microstructures. Here, the through-thickness z-direction and in-plane x-direction are highlighted. Based on oblate-shaped particles with fixed reactive area density but decreasing degree of morphological texture, inset (i) corresponds to ∞ MRD, (ii) to 3.55 MRD and (iii) to 10 MRD. Microstructure (iv) has a higher aspect ratio than microstructure (i), while microstructure (v) is comprised of perfectly aligned prolate-shaped particles. Overall, microstructures based on prolate and oblate-shaped particles span overlapping regions of the Bruggeman exponent-normalized area density space and thus enable one to choose the underlying particle shape-based on other factors such as ease of morphology fabrication, given the underlying active material specific degradation mechanisms and manufacturing cost.

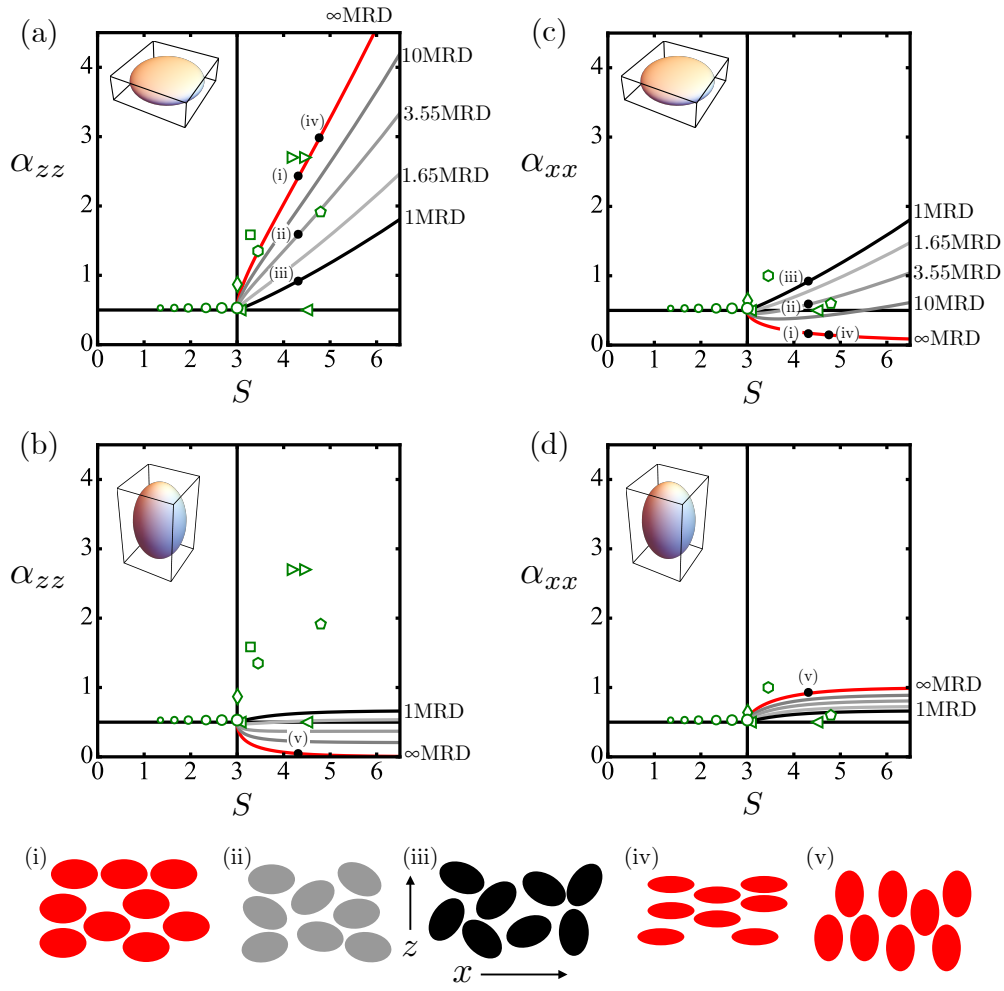

Figure S2: Through-thickness Bruggeman exponent as a function of normalized reaction area density for porous electrode microstructures of (a) oblate and (b) prolate particle morphologies, while in-plane Bruggeman exponent as a function of normalized reaction area density for porous electrode microstructures correspond to (c) for oblate and to (d) for prolate particle morphologies. Representative three dimensional particle morphologies are shown in the upper left corner of the plots. Symbols correspond to common battery materials as reported in scientific literature: ◁ corresponds to pollen derived spiky carbon particles prepared by Pol and coworkers [4]; ⬡ corresponds to values reported by Shearing *et al.* for LFP [5]; ▷ corresponds to jammed systems of tetrahedra as reported by Smith and Fisher [6]; □ corresponds to LMO particles as reported by Gupta, Shyy, and coworkers [7]; ⬠ corresponds to aligned graphite particles, ◇ corresponds to LCO porous electrodes and ○ corresponds to NMC porous electrodes as reported by Ebner, Chung, and coworkers [3]. Decreasing size of symbols indicates increasing degree of polydispersity. The point $(\alpha = 3, S = 0.5)$ corresponds to a porous microstructure of monodispersed random distribution of spherical particles. Away from perfectly spherical particles, the particle aspect ratio increases along lines of constant MRD. The red curve represents perfectly aligned ellipsoids, the black curve represents randomly oriented ellipsoids while the grey curves represents ellipsoids with intermediate MRD values. Schematics for representative microstructures based on ellipsoid-shaped particles are shown in insets (i) through (iv). Through thickness z-direction corresponds to the vertical direction while the in-plane x-direction corresponds to the horizontal direction.

3 Effect of Dual Porosity

Figure S3 (a) shows the effect of dual porous design on a LCO-based porous electrode microstructure, as reported experimentally by Ebner, Chung, and coworkers [3]. The channel volume fraction ϵ_c increases along the blue lines. For a fixed matrix porosity ϵ, through-thickness Bruggeman exponent decreases with increasing ϵ_c at the expense of total reactive area and volume fraction of active material in agreement with Bae *et al.* [8]. As the matrix porosity decreases, the drop in the through-thickness Bruggeman exponent becomes more apparent.

The in-plane Bruggeman exponent of dual porous microstructures is a function of the morphology and spatial distribution of the channels. However, an upper bound for the in-plane Bruggeman exponent can be obtained by treating the channels and matrix as a series combination of resistors, $\tau_T/\epsilon_T = 1/\epsilon_T^{1+\alpha_T} = \epsilon_c + (1-\epsilon_c)/\epsilon^{1+\alpha_{xx}}$, see Figure S3 (b)[1]. Such dual porous microstructures have recently been made by Delattre and co-workers [9].

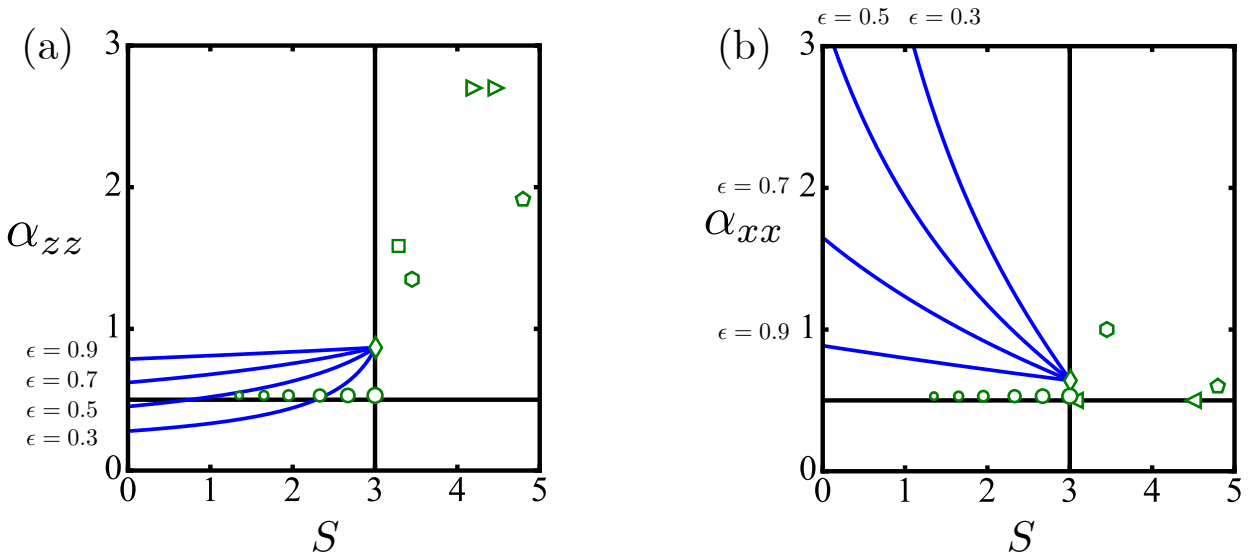

Figure S3: Effect of dual porous architecture on the a) through-thickness and b) in-plane Bruggeman exponents as a function of normalized area density for a LCO-based porous electrode microstructure. The Bruggeman exponent is a function of the matrix porosity and the volume fraction of the channels. Each blue curve corresponds to a fixed porosity of the matrix as shown. Moving along a blue curve from right to left corresponds to increasing channel volume fraction. Symbols represent common battery materials as reported in scientific literature: ◁ corresponds to pollen derived spiky carbon particles prepared by Pol and coworkers [4]; ⬡ corresponds to values reported by Shearing *et al.* for LFP [5]; ▷ corresponds to jammed systems of tetrahedra as reported by Smith and Fisher [6]; □ corresponds to LMO as reported by Gupta, Shyy and coworkers [7]; ⬠ corresponds to aligned graphite particles, ◇ corresponds to LCO porous electrodes and ○ corresponds to NMC porous electrodes as reported by Ebner, Chung, and coworkers [3].

The effect of a dual porous design on the Bruggeman exponents and normalized area densities of commer-

[1]For dual porous microstructures, α_T and S_T are used in place of α_{xx} and S in Figures S3 (b) and S4 (b).

cial microstructures is shown in Figure S4. The design that spans the largest area of Bruggeman exponent area density space is obtained by microstructures with a high through-thickness matrix Bruggeman exponent and area density (such as graphite).

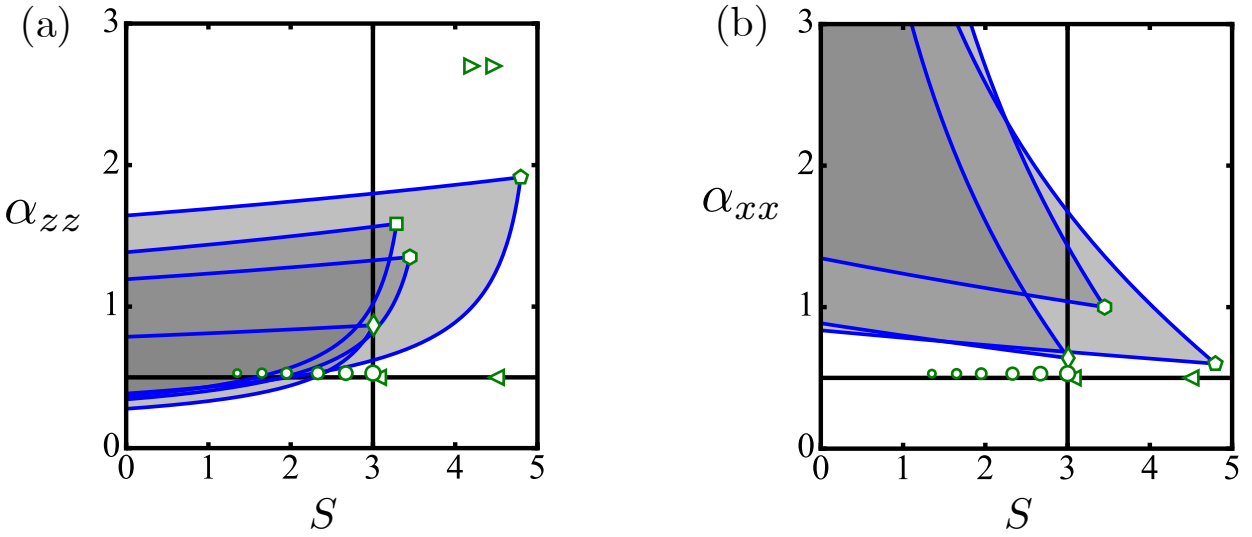

Figure S4: Effect of dual porous architecture on the a) through-thickness and b) in-plane Bruggeman exponents as a function of normalized area density for porous electrodes of various chemistries. Symbols represent common battery materials as reported in scientific literature: ◁ corresponds to pollen derived spiky carbon particles prepared by Pol and coworkers [4]; ⬡ corresponds to values reported by Shearing *et al.* for LFP [5]; ▷ corresponds to jammed systems of tetrahedra as reported by Smith and Fisher [6]; □ corresponds to LMO as reported by Gupta, Shyy and coworkers [7]; ⬠ corresponds to aligned graphite particles, ◇ corresponds to LCO porous electrodes and ○ corresponds to NMC porous electrodes as reported by Ebner, Chung, and coworkers [3]. The shaded region between the blue curves for each chemistry represents the region of the Bruggeman exponent - normalized area density space that can be spanned by a dual porous architecture of matrix porosity between 0.3 and 0.9. High through-thickness tortuosity and area density microstructures such as graphite offer more flexibility in design.

4 Effect of Thickness and Porosity

Figure S5 (a) shows the effect of decreasing the thickness of the anode layer from 100 μm to 57.47 μm, and the thickness of the cathode layer from 172.41 μm to 100 μm, while keeping the theoretical capacity ratio fixed. Thinner electrodes decrease diffusion distances thereby resulting in a higher power densities. Figure S5 (c) shows the effect of increasing the thickness of the anode layer from 100 μm to 172.41 μm and the cathode layer thickness from 174 μm to 300 μm while keeping the theoretical capacity ratio fixed. Thicker electrodes increase diffusion distances thereby resulting in lower power densities. Simulations show that thinner cells based on spherical particles and polyhedra-based colloidal microstructures are beneficial for high power density applications, while thicker electrochemical cells based on high aspect ratio particle morphologies are suitable for high energy density applications.

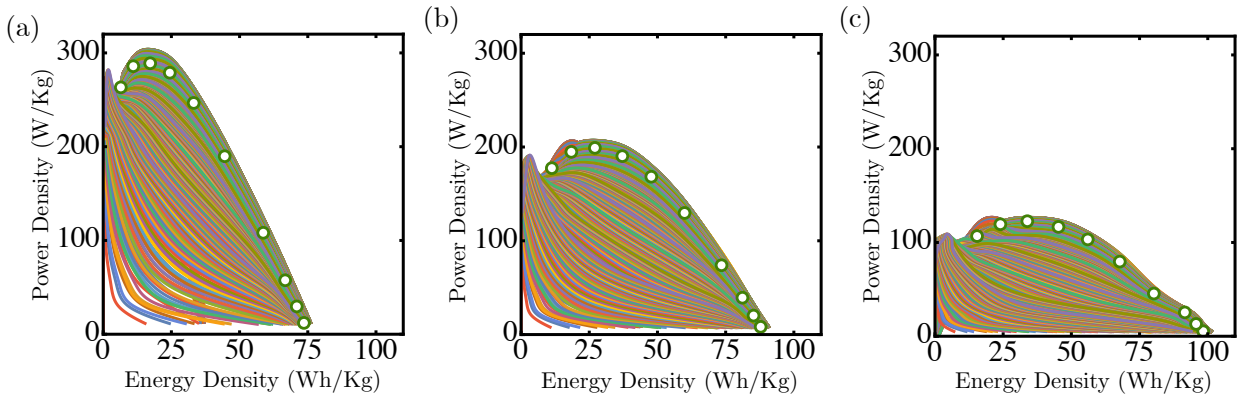

Figure S5: Combined effect of electrode thickness and cathode microstructure on the Ragone response for Li_xC_6 | LMO porous cell, as reported in Table S1 while keeping the capacity ratio constant. Inset (a) corresponds to an anode thickness of 57.47 μm and cathode thickness of 100 μm. Inset (b) is reproduced from Figure 5 (e) as reference and corresponds to an anode thickness of 100 μm and cathode thickness of 174 μm. Inset (c) corresponds to an anode thickness of 172.41 μm and cathode thickness of 300 μm. Increasing the size of the cell increases diffusion distances thereby increasing energy density at the expense of power density.

Figure S6 (b) shows the effect of increasing the cathode porosity from $\epsilon = 0.707$ to $\epsilon = 0.8$ on the power and energy density. Larger cathode porosities allow faster lithium diffusion while decreasing underutilized mass of the cathode. As a result, both energy and power densities increase. This phenomenon is enhanced when the cathode porosity is further increased from $\epsilon = 0.707$ to $\epsilon = 0.9$ as shown in Figure S6 (c). However, microstructures based on spherical particles display a marked drop in the Ragone plot response as the cathode porosity is increased because total electrochemically active area and volume fraction of active material significantly decreases. Such effect leads to reduced power densities. Therefore, battery architectures based on high aspect ratio morphologies, both prolate and oblate, benefit from increased porosity.

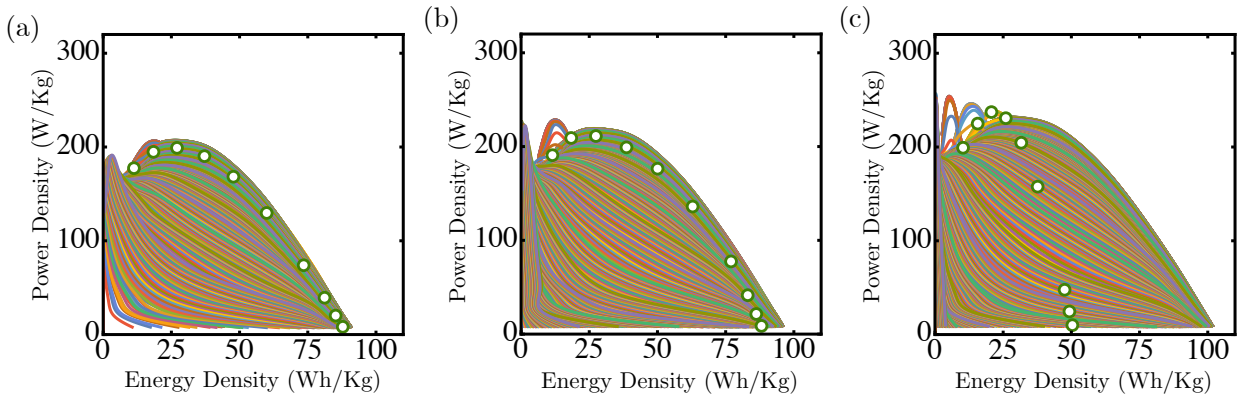

Figure S6: Combined effect of cathode porosity and microstructure on the Ragone response for Li_xC_6 | LMO porous cell, as reported in Table S1. Inset (a) is reproduced from Figure 5 (e) as reference and corresponds to a cathode porosity of $\epsilon = 0.707$. Inset (b) corresponds to a cathode porosity of $\epsilon = 0.8$. Inset (c) corresponds to a cathode porosity of $\epsilon = 0.9$. Increasing the cathode porosity leads to faster transport of lithium across the cell thereby increasing the power density. Increasing the porosity also balances the maximum lithium capacity of the anode and the cathode thereby increasing the energy density.

References

[1] M. Doyle, J. Newman, A. S. Gozdz, C. N. Schmutz and J.-M. Tarascon, *Journal of the Electrochemical Society*, 1996, **143**, 1890–1903.

[2] T. F. Fuller, M. Doyle and J. Newman, *Journal of the Electrochemical Society*, 1994, **141**, 1–10.

[3] M. Ebner, D. W. Chung, R. E. García and V. Wood, *Advanced Energy Materials*, 2014, **4**, 1–6.

[4] J. Tang, V. Etacheri and V. G. Pol, *Scientific Reports*, 2016, **6**, 20290.

[5] S. J. Cooper, D. S. Eastwood, J. Gelb, G. Damblanc, D. J. L. Brett, R. S. Bradley, P. J. Withers, P. D. Lee, A. J. Marquis, N. P. Brandon and P. R. Shearing, *Journal of Power Sources*, 2014, **247**, 1033–1039.

[6] K. C. Smith and T. S. Fisher, *Journal of Heat Transfer*, 2013, **135**, 081301.

[7] A. Gupta, J. H. Seo, X. Zhang, W. Du, A. M. Sastry and W. Shyy, *Journal of The Electrochemical Society*, 2011, **158**, A487.

[8] C. J. Bae, C. K. Erdonmez, J. W. Halloran and Y. M. Chiang, *Advanced Materials*, 2013, **25**, 1254–1258.

[9] B. Delattre, R. Amin, J. Sander, J. De Coninck, A. P. Tomsia and Y.-M. Chiang, *Journal of the Electrochemical Society*, 2018, **165**, A388–A395.